

# Pixelwise Uncertainty Quantification of Accelerated MRI Reconstruction

Ilias I. Giannakopoulos, *Senior Member, IEEE*, Lokesh B Gautham Muthukumar, Yvonne W. Lui, and Riccardo Lattanzi, *Senior Member, IEEE*

**Abstract**—Parallel imaging techniques reduce magnetic resonance imaging (MRI) scan time but image quality degrades as the acceleration factor increases. In clinical practice, conservative acceleration factors are chosen because no mechanism exists to automatically assess the diagnostic quality of undersampled reconstructions. This work introduces a general framework for pixel-wise uncertainty quantification in parallel MRI reconstructions, enabling automatic identification of unreliable regions without access to any ground-truth reference image. Our method integrates conformal quantile regression with image reconstruction methods to estimate statistically rigorous pixel-wise uncertainty intervals. We trained and evaluated our model on Cartesian undersampled brain and knee data obtained from the fastMRI dataset using acceleration factors ranging from 2 to 10. An end-to-end Variational Network was used for image reconstruction. Quantitative experiments demonstrate strong agreement between predicted uncertainty maps and true reconstruction error. Using our method, the corresponding Pearson correlation coefficient was higher than 90% at acceleration levels at and above four-fold; whereas it dropped to less than 70% when the uncertainty was computed using a simpler a heuristic notion (magnitude of the residual). Qualitative examples further show the uncertainty maps based on quantile regression capture the magnitude and spatial distribution of reconstruction errors across acceleration factors, with regions of elevated uncertainty aligning with pathologies and artifacts. The proposed framework enables evaluation of reconstruction quality without access to fully-sampled ground-truth reference images. It represents a step toward adaptive MRI acquisition protocols that may be able to dynamically balance scan time and diagnostic reliability.

**Index Terms**—Conformal Prediction, Magnetic Resonance Imaging, Parallel Imaging, Quantile Regression, Uncertainty Quantification

## I. INTRODUCTION

This work was supported in part by NIH K99 EB035163, in part by NIH R01 EB024536, and was performed under the Rubric of the Center for Advanced Imaging Innovation and Research (CAI<sup>2</sup>R, [www.cai2r.net](http://www.cai2r.net)), an NIBIB National Center for Biomedical Imaging and Bioengineering (NIH P41 EB017183).

Ilias I. Giannakopoulos, Lokesh B Gautham Muthukumar, Yvonne W. Lui, and Riccardo Lattanzi are with the Bernard and Irene Schwartz Center for Biomedical Imaging, Department of Radiology, NYU Grossman School of Medicine, 10016, New York, NY, United States of America (e-mail: [iliias.giannakopoulos@nyulangone.org](mailto:iliias.giannakopoulos@nyulangone.org), [LokeshGautham.BoominathanMuthukumar@nyulangone.org](mailto:LokeshGautham.BoominathanMuthukumar@nyulangone.org), [yvonne.lui@nyulangone.org](mailto:yvonne.lui@nyulangone.org), [riccardo.lattanzi@nyulangone.org](mailto:riccardo.lattanzi@nyulangone.org)).

Lokesh B Gautham Muthukumar is also with the Courant Institute of Mathematical Sciences, NYU, 10012, New York, NY, United States of America.

Yvonne W. Lui and Riccardo Lattanzi are also with the Center for Advanced Imaging Innovation and Research (CAI<sup>2</sup>R), Department of Radiology, NYU Grossman School of Medicine, 10016, New York, NY, United States of America.

MAGNETIC resonance imaging (MRI) provides unparalleled soft-tissue contrast and plays a central role in modern disease diagnostics. However, its high diagnostic value is counterbalanced by inherently long acquisition times, which limit patient throughput, increase susceptibility to motion artifacts, reduce patient comfort, and systemically, raise operational costs and decrease accessibility. Rapid MRI techniques, such as parallel imaging (PI) [2]–[4] and compressed sensing (CS) [5], [6], can mitigate these limitations by reconstructing images from undersampled k-space data. More recently, deep learning-based unrolled reconstruction networks achieved superior reconstruction quality compared with traditional methods [1], [7]–[12]. Clinical evaluation studies demonstrated that these networks produce diagnostically interchangeable reconstructions equivalent to fully sampled references at four-fold acceleration [12]–[15], which led to their recent U.S. Food and Drug Administration (FDA) clearance. Diagnostic quality can be maintained even at higher accelerations in certain cases. For example, the study in [16] reported that 100% of 4 $\times$ , 97% of 6 $\times$ , 62% of 8 $\times$ , 17% of 10 $\times$ , and 3% of 12 $\times$  accelerated T2-weighted images reconstructed using the end-to-end variational network (E2E VarNet) [1] are appropriate for general-purpose diagnostic imaging. For healthy subjects, 10 $\times$  acceleration factor can result in acceptable images, as these networks are primarily trained on cases without pathologies [17]. This suggests that some fraction of MRI scans performed today could, in principle, be done faster than what current conservative, fixed-acceleration protocols allow.

Despite the potential for faster scans, high acceleration levels are not routinely implemented in clinical MRI protocols. The primary limiting factor is the absence of an automatic mechanism to assess the reliability of reconstructed images when no fully sampled reference is available. Without a quantitative measure of confidence, increasing the acceleration factor beyond established values is risky, as undersampling may lead to network hallucinations [18] or pathological feature suppression [19], ultimately compromising diagnostic accuracy. Consequently, current clinical practice favors conservative, fixed acceleration factors, typically set to two for non-learning-based reconstructions [3] and four for learning-based reconstructions [1]. To enable higher accelerations while preserving diagnostic validity, there is a critical need for methods capable of estimating the reconstruction error directly from undersampled data. Uncertainty quantification [20]–[22] provides a principled framework toward that goal by estimating confidence intervals for reconstructed images and effectively producing an “error map” when the ground-truth

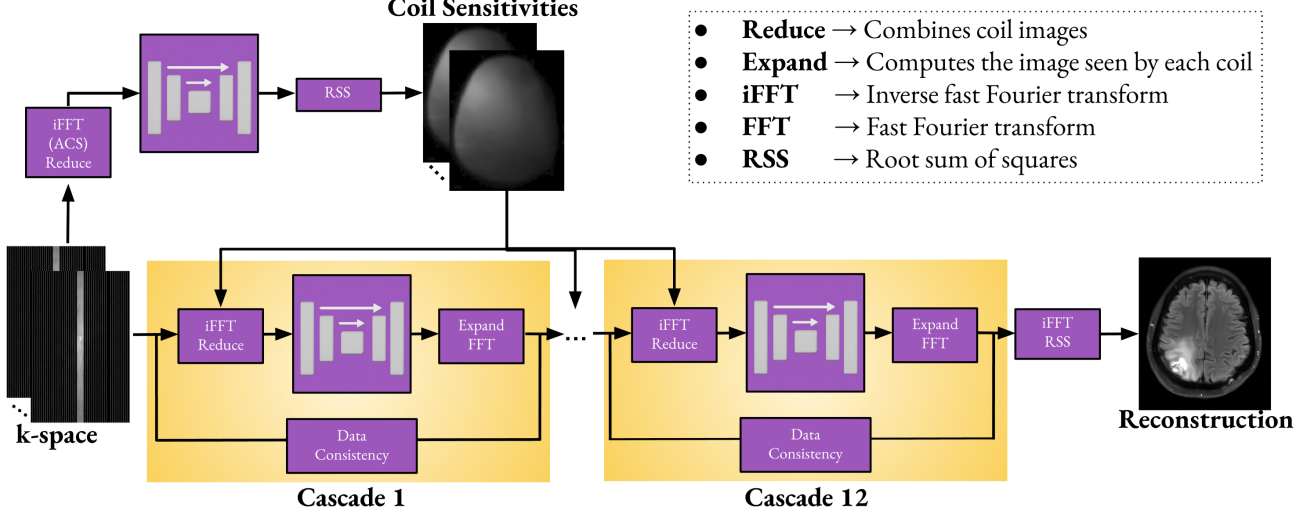


Fig. 1. E2E VarNet architecture. The input is the undersampled multi-coil k-space and the output is the reconstructed image. In each cascade, the inverse fast Fourier transform (iFFT) is applied to each undersampled k-space, and the resulting images are weighted with the corresponding coil sensitivities and are combined into a single image using the *reduce operator* [1]. The combined image is processed by a U-Net, whose output is then expanded [1] back into individual coil images. These coil images are transformed to k-space using the FFT, after which data consistency is enforced. The final image is obtained using the root sum of squares (RSS) on the individual coil images obtained from the 12<sup>th</sup> cascade.

reference image is unavailable.

Early attempts to quantify uncertainty in MRI reconstructions were based on probabilistic formulations of deep reconstruction networks. For example, [23] proposed a variational autoencoder framework that learns to predict pixel-wise residual magnitudes for a pre-trained reconstruction network. The resulting uncertainty maps provide a useful visualization of reconstruction reliability, but the approach remains heuristic and lacks statistical guarantees on the predicted uncertainty levels. In [24], a Bayesian heteroscedastic uncertainty framework is used to highlight regions of potential reconstruction failure, but does not yield calibrated or distribution-free confidence intervals. The work in [25] introduced a Bayesian variational formulation of the learned variational network, in which the parameters of the regularizer are modeled as random variables drawn from a learned multivariate Gaussian distribution. Sampling these parameters enables estimation of pixel-wise variance maps that reflect regions of high uncertainty. While this framework offers a theoretically grounded means of visualizing uncertainty, it incurs substantial computational overhead and does not ensure calibrated or interpretable confidence intervals. PixCUE [26] reformulated MRI reconstruction as a pixel-classification problem, where uncertainty is derived from the variance of the softmax output distribution. While this approach enables efficient joint estimation of reconstruction and uncertainty, it remains heuristic and lacks statistical calibration or formal coverage guarantees.

A major advance toward statistically valid uncertainty estimation came with the work of [22], who introduced a distribution-free framework for image-to-image regression based on conformal prediction. The proposed methods produce pixel-wise uncertainty intervals with finite-sample coverage guarantees by calibrating heuristic uncertainty estimates on a held-out calibration dataset. [27] applied this approach to MRI

reconstruction using the magnitude of the residual (ResM) as an uncertainty estimator. Despite encouraging results, ResM yields symmetric confidence bounds that limit interpretability and can inflate the estimated uncertainty range. Moreover, the residuals learned during training are often smaller than those encountered during testing, leading to unreliable uncertainty estimates that correlate poorly with the true reconstruction error [22].

In the present work, we propose a statistically rigorous uncertainty estimation framework based on conformalized quantile regression (QR) [22] that can be incorporated as an add-on module to any image reconstruction method. The proposed module directly estimates the conditional quantiles of the reconstructed image distribution, thereby producing statistically valid and spatially resolved uncertainty intervals. A similar QR-based strategy has recently been applied in CUTE-MRI [28], where conformal calibration is used to control uncertainty in downstream clinical metrics to enable time-adaptive acquisitions. In contrast, our work focuses on pixel-wise uncertainty estimation of the reconstructed image itself, providing spatially localized confidence maps.

## II. METHODS

### A. Dataset

Data used in this work were obtained from the NYU fastMRI Initiative database (fastmri.med.nyu.edu) [29], [30]. We used both the brain and knee fastMRI datasets. For brain experiments, the networks were trained on the fastMRI brain training dataset (4469 volumes). The fastMRI brain validation dataset (1378 volumes) was randomly divided into two equal subsets for validation and calibration (689 volumes each; see Section II-D4). The full brain test dataset (558 volumes) was used for testing. For the knee experiments, networks were trained on the fastMRI knee training dataset (973 volumes).

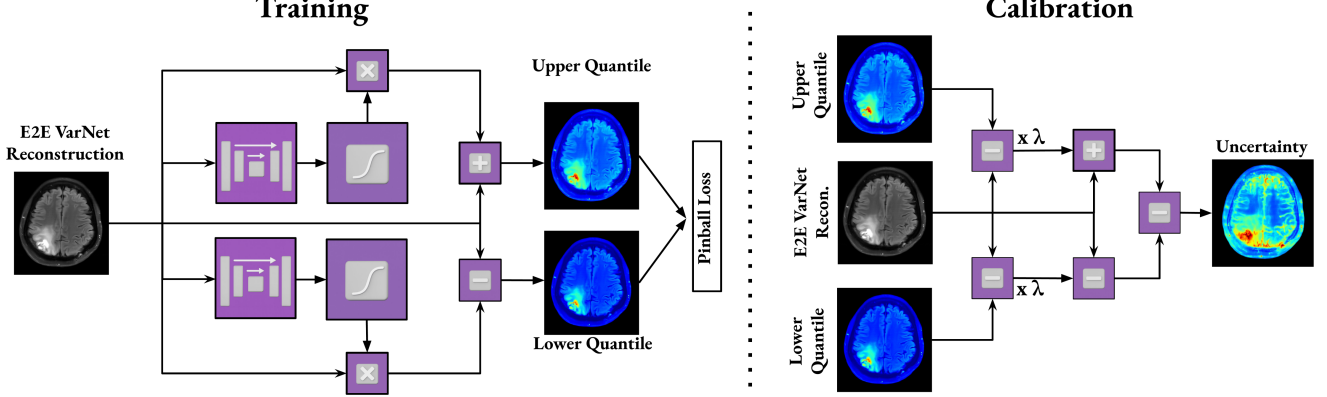


Fig. 2. (Left) Architecture of our proposed uncertainty estimation module. The output (reconstructed MR image) of the E2E VarNet is the input of two U-Nets, which learn pixelwise offsets that parameterize the lower and upper quantile bounds of the reconstruction uncertainty. Each U-Net output passes through a sigmoid activation, is multiplied by the E2E VarNet reconstruction, and is either added to or subtracted from the E2E VarNet's reconstruction to compute the upper and lower bound, respectively. The output that is added is treated as the upper quantile interval and the one that is subtracted is the lower quantile interval. (Right) In Calibration, the predicted offsets are scaled by the calibration factor  $\lambda$  which is computed using conformal prediction in the calibration set. The uncertainty map is computed by subtracting the calibrated lower from the calibrated upper bound.

TABLE I  
MEAN AND STANDARD DEVIATION OF SSIM AND UNCERTAINTY

Acceleration	2×			4×			6×			8×			10×	
	Metric	SSIM	QR (%)	SSIM	QR (%)	ResM (%)	SSIM	QR (%)	SSIM	QR (%)	SSIM	QR (%)	SSIM	QR (%)
<b>T1</b>	0.979	$2.1 \pm 0.82$	0.966	$3.4 \pm 1.85$	$3.8 \pm 1.82$	0.960	$4.0 \pm 2.54$	0.954	$4.8 \pm 3.61$	0.950	$5.4 \pm 4.29$			
<b>T1PRE</b>	0.971	$2.6 \pm 1.00$	0.956	$4.0 \pm 1.99$	$4.3 \pm 2.36$	0.949	$4.7 \pm 2.73$	0.942	$5.6 \pm 3.88$	0.937	$6.4 \pm 4.74$			
<b>T1POST</b>	0.980	$2.2 \pm 0.87$	0.965	$3.7 \pm 2.18$	$3.3 \pm 1.94$	0.957	$4.4 \pm 3.06$	0.950	$5.4 \pm 4.35$	0.944	$6.2 \pm 5.34$			
<b>T2</b>	0.974	$2.6 \pm 1.65$	0.959	$4.1 \pm 2.84$	$4.0 \pm 2.71$	0.951	$5.0 \pm 3.67$	0.945	$6.1 \pm 5.10$	0.940	$7.0 \pm 6.17$			
<b>FLAIR</b>	0.957	$3.4 \pm 1.46$	0.931	$5.3 \pm 2.75$	$6.2 \pm 3.55$	0.919	$6.1 \pm 3.58$	0.909	$7.3 \pm 4.84$	0.902	$8.3 \pm 5.76$			
<b>Knee</b>	-	-	0.927	$4.6 \pm 2.15$	$3.9 \pm 2.18$	0.911	$6.3 \pm 3.05$	-	-	-	-			

Since the ground-truth reference images are not available in the fastMRI knee test dataset, we divided the knee validation dataset into 49 volumes for validation, 50 for calibration, and 99 for testing.

### B. Undersampling Strategy

Cartesian undersampling was used for all experiments. For the brain dataset, we retained 16%, 8%, 5.3%, 4%, or 3% of the central k-space as autocalibration signal (ACS) lines and uniformly sampled the remaining k-space to achieve acceleration factors of 2, 4, 6, 8, and 10, respectively. All models were trained and tested using fixed undersampling masks, resulting in five separate models for reconstruction. For the knee dataset, 8% or 5.3% of the central k-space was retained as ACS lines, and the remaining k-space was uniformly sampled to achieve an acceleration factor of 4 or 6, respectively, resulting in two separate models for reconstruction.

### C. Baseline Reconstruction Network

We used the E2E VarNet as our image reconstruction method [1]. The model's architecture is shown in the top panel of Figure 1. We used a total of 12 cascades. In each cascade, the U-Net [31] used 32 feature channels, 4 layers of average pooling and transpose convolutions, each with a kernel size, stride, and padding of 2, 2, and 0, respectively. The

convolution layers used a kernel size of 3 with both padding and stride set to 1. Leaky ReLU activation functions were used with a negative slope of 0.2. The U-Net for the coil sensitivity estimation had the same parameters except the number of channels which was reduced to 8. The input tensors to all U-Nets were normalized to ensure that each channel had a mean of 0 and a standard deviation of 1. We used a batch size of 1 and trained on a high-performance computing cluster using four NVIDIA A100 Tensor Core GPUs, each with 80 GB of memory. Our loss function was the structural similarity index measure (SSIM) [32]. Training was performed using the AdamW optimizer with a learning rate of 0.0003 for 210,000 iteration steps. A warm-up ramp was applied during the first 7,500 steps, followed by cosine annealing after 140,000 steps. The overall number of trainable parameters was 93.6 million and the training times was approximately two and a half days for all models.

### D. Uncertainty Estimation Framework

1) *Uncertainty Module Architecture*: Our uncertainty estimation module architecture is shown in Figure 2 (left). The output reconstruction of the E2E VarNet is used as the input to this module. The architecture consists of two U-Nets with the same settings as those used in the E2E VarNet cascades, except that the number of input and output channels is set to 1 (real data) instead of 2 (complex data). Each U-Net

output passes through a sigmoid activation to scale the values between 0 and 1, after which it is multiplied by the E2E VarNet reconstruction to match the same intensity range as the reconstructed image. The resulting outputs are used as the upper and lower quantile intervals, respectively. When symmetric upper and lower quantiles are desired, a single U-Net can be used.

2) *Pixelwise Quantile Regression Training*: The two U-Nets described above directly parameterize the pixelwise lower and upper quantile functions  $\tilde{l}(\mathbf{x})$  and  $\tilde{u}(\mathbf{x})$ , and are trained using QR with the quantile loss. In pixelwise QR [33], [34], assuming we target an  $\alpha$ -level uncertainty interval of the E2E VarNet reconstructed image  $(\mathbf{x})$ , the upper quantile  $\tilde{u}(\mathbf{x})$  is trained to estimate the  $(1 - \alpha/2)$  conditional quantile, and the lower quantile  $\tilde{l}(\mathbf{x})$  to estimate the  $(\alpha/2)$  conditional quantile. These pixelwise quantiles can be estimated using the quantile (pinball) loss [22], defined as

$$\mathcal{L}_\alpha(\hat{q}_\alpha(\mathbf{x}), \mathbf{y}) = \begin{cases} \alpha(\mathbf{y} - \hat{q}_\alpha(\mathbf{x})), & \text{if } \mathbf{y} > \hat{q}_\alpha(\mathbf{x}), \\ (1 - \alpha)(\hat{q}_\alpha(\mathbf{x}) - \mathbf{y}), & \text{otherwise.} \end{cases} \quad (1)$$

Here,  $\mathbf{y}$  denotes the ground-truth reference image and  $\hat{q}_\alpha(\mathbf{x})$  denotes the predicted  $\alpha$ -quantile of  $\mathbf{y}$  conditioned on  $\mathbf{x}$ . Because the upper and lower quantiles correspond to different conditional quantiles, they are trained using separate losses. The total loss is therefore written as

$$\mathcal{L}(\mathbf{x}, \mathbf{y}) = \mathcal{L}_{\alpha/2}(\tilde{l}(\mathbf{x}), \mathbf{y}) + \mathcal{L}_{1-\alpha/2}(\tilde{u}(\mathbf{x}), \mathbf{y}). \quad (2)$$

After training, the lower and upper quantile estimates are expected to converge asymptotically [33], [35]–[39] to the true conditional  $(\alpha/2)$ -and  $(1 - \alpha/2)$ -quantiles, respectively.

Training is performed in a supervised manner using  $(\mathbf{x}, \mathbf{y})$  pairs. The uncertainty module is trained separately from the E2E VarNet, using the same optimizer, learning rate, scheduler, and hyperparameters. The E2E VarNet is kept frozen. During reconstruction, one can either use the E2E VarNet to generate reconstructions on the fly, or the reconstructions can be pre-computed for all training and validation data and loaded from memory. We set  $\alpha = 90\%$  for all experiments. The number of trainable parameters was 15.5 million and the training time was approximately one day for all models.

3) *Magnitude of the Residual Training*: For the ResM-based approach, we assumed that  $\tilde{u}(\mathbf{x}) = \tilde{l}(\mathbf{x})$ . The loss function used in the case is written as:

$$\mathcal{L}(\mathbf{x}, \mathbf{y}) = (\tilde{u}(\mathbf{x}) - |\mathbf{x} - \mathbf{y}|)^2. \quad (3)$$

The number of trainable parameters in the ResM case was 7.75 million and the training time was approximately one day for both anatomies.

4) *Conformal Prediction Calibration*: The quantile estimates  $\tilde{l}$  and  $\tilde{u}$  must be calibrated to be statistically valid, meaning that the resulting uncertainty intervals should contain at least a fraction  $(1 - \alpha)$  of the ground-truth pixel values with probability not smaller than  $(1 - \alpha)$ . In practice, neural networks trained to predict quantiles may produce intervals that are miscalibrated, either too narrow or too wide. To guarantee valid coverage, we apply conformal prediction calibration [22], [40], as in Figure 2 (right).

In particular, we rescaled the predicted offsets between the reconstructed image  $\mathbf{x}$  and the learned quantiles using a data-driven correction factor  $\lambda$ . In standard conformal QR [22], the quantiles themselves are rescaled. However, because our architecture 2 scales the U-Net outputs with the images, the natural quantities to calibrate are the offsets  $(\mathbf{x} - \tilde{l})$  and  $(\tilde{u} - \mathbf{x})$ . To perform the calibration, we start by defining the pixelwise uncertainty interval for pixel  $(m, n)$  of  $\mathbf{x}$  as:

$$\begin{aligned} \mathcal{T}_\lambda(\mathbf{x}_{(m,n)}) &= [\tilde{l}_b, \tilde{u}_b] \\ \tilde{l}_b &= \mathbf{x}_{(m,n)} - \lambda \cdot (\mathbf{x}_{(m,n)} - \tilde{l}(\mathbf{x}_{(m,n)})) \\ \tilde{u}_b &= \mathbf{x}_{(m,n)} + \lambda \cdot (\tilde{u}(\mathbf{x}_{(m,n)}) - \mathbf{x}_{(m,n)}). \end{aligned} \quad (4)$$

Then, we seek the smallest  $\lambda$  such that  $\mathcal{T}_\lambda$  achieves the desired coverage. This is computed using a held-out calibration dataset of  $I$  image pairs  $\{(\mathbf{x}^i, \mathbf{y}^i)\}_{i=1}^I$ , where  $\mathbf{x}^i$  are reconstructions from the E2E VarNet and  $\mathbf{y}^i$  are the corresponding ground-truth images. The value of  $\lambda$  is chosen such that the average fraction of all pixels  $(m, n)$  across the calibration set whose ground-truth intensities fall outside their corresponding intervals  $\mathcal{T}_\lambda(\mathbf{x}_{(m,n)}^i)$  does not exceed  $\alpha$ . Since this fraction is estimated from a finite calibration set, a conservative upper bound  $\hat{R}^+(\lambda)$  is used following Hoeffding's inequality [41]. The final calibrated scaling factor is therefore given by

$$\min \left\{ \lambda : \hat{R}^+(\lambda) \leq \alpha \right\}. \quad (5)$$

The calibration required roughly 6 hours for each brain model and 3 hours for each knee model. The calibrated scaling factors for the brain and QR-based uncertainty were 1.31, 1.54, 1.59, 1.74, and 1.87 for  $2\times$ ,  $4\times$ ,  $6\times$ ,  $8\times$ , and  $10\times$  acceleration, respectively. For the ResM-based uncertainty, the scaling factor at  $4\times$  acceleration was 1.02. For the knee, the scaling factors for the QR-based uncertainty were 1.42 and 1.68 for  $4\times$  and  $6\times$  acceleration, respectively. For the ResM-based uncertainty, the scaling factor at  $4\times$  acceleration was 0.82.

### E. Evaluation of Uncertainty Reliability

To assess the correspondence between the predicted uncertainty and the true reconstruction error, we define the uncertainty map  $\tilde{q}$  and the absolute error map  $\tilde{e}$  as

$$\tilde{q} = \tilde{u}_b(\mathbf{x}) - \tilde{l}_b(\mathbf{x}), \quad \tilde{e} = |\mathbf{x} - \mathbf{y}|, \quad (6)$$

The map  $\tilde{q}$  quantifies the pixelwise uncertainty width, while  $\tilde{e}$  represents the magnitude of the absolute (true) reconstruction error. Notice that  $\tilde{q}$  does not have any knowledge of the ground-truth  $\mathbf{y}$ .

1) *Correlation Metrics*: The correspondence between the predicted uncertainty  $\tilde{q}$  and the true error  $\tilde{e}$  is quantified using the Pearson [42] and Spearman [43] correlation coefficients. The Pearson correlation coefficient measures the linear association between  $\tilde{q}$  and  $\tilde{e}$  and is defined as

$$r = \frac{\text{cov}(\tilde{q}, \tilde{e})}{\sigma_{\tilde{q}}\sigma_{\tilde{e}}}, \quad (7)$$

where  $\text{cov}$  denotes the covariance.

The Spearman rank correlation coefficient quantifies whether pixels with higher predicted uncertainty also tend to have higher reconstruction errors, independent of their exact numerical scaling. It is computed by applying the Pearson correlation to the rank-ordered variables, where each pixel value in  $\tilde{q}$  and  $\tilde{e}$  is replaced by its position in the sorted list of all pixel values within the image, yielding  $R_{\tilde{q}}$  and  $R_{\tilde{e}}$ , respectively. The coefficient is then computed as

$$\rho = \frac{\text{cov}(R_{\tilde{q}}, R_{\tilde{e}})}{\sigma_{R_{\tilde{q}}} \sigma_{R_{\tilde{e}}}}. \quad (8)$$

Here,  $R_{\tilde{q}}$  and  $R_{\tilde{e}}$  denote the rank-ordered maps, in which lower pixel values receive smaller ranks and higher pixel values receive larger ranks.

In addition to global correlations, we also computed region-based Pearson and Spearman correlations to assess whether uncertainty reflects local reconstruction errors. Each image was divided into 100 non-overlapping patches of approximately equal size, and the correlation metrics were computed within each patch and averaged across all regions.

Before computing correlation metrics, both  $\tilde{q}$  and  $\tilde{e}$  were blurred using a Gaussian filter with a standard deviation of  $\sigma = 2$  to suppress pixel-level noise and emphasize spatially coherent patterns.

### III. RESULTS

#### A. Quantitative assessment of uncertainty

Table I reports the mean and standard deviation of the SSIM between the reconstruction and the ground-truth, as well as the mean and standard deviation of the uncertainty values estimated by our model for acceleration factors of  $2\times$ ,  $4\times$ ,  $6\times$ ,  $8\times$ , and  $10\times$  for each contrast in the brain test dataset and for acceleration factors of  $4\times$  and  $6\times$  for the knee test dataset. The reported uncertainty values represent the average width of the calibrated pixelwise uncertainty intervals, normalized by the maximum reconstruction magnitude, and therefore quantify the relative scale of the predicted reconstruction error as a percentage of the image intensity. For the  $4\times$  accelerated reconstructions, we compared QR-based and ResM-based uncertainties. Both methods yielded comparable ranges for the uncertainty estimates. All uncertainty maps were normalized by the maximum reconstruction magnitude to express values as percentages. All values were computed per volumetric case.

Table II reports Pearson and Spearman correlation coefficients (including region-based) between the predicted uncertainty and the true reconstruction error for the brain ( $2\times$ ,  $4\times$ ,  $6\times$ ,  $8\times$ , and  $10\times$  acceleration factors) and the knee test datasets ( $4\times$  and  $6\times$  acceleration factors). For the  $4\times$  accelerated reconstructions, we also computed the correlation coefficients between the ResM-based uncertainty and the true reconstruction error.

Figure 3 shows the distribution of the Pearson correlation for all test data between the predicted uncertainty and the true reconstruction error for the  $4\times$  undersampled brain (top) and knee (bottom) test dataset. Each bar represents the number of cases achieving a given correlation level. The QR-based estimates (blue) are consistently higher than the ResM-based ones (red) for both anatomies.

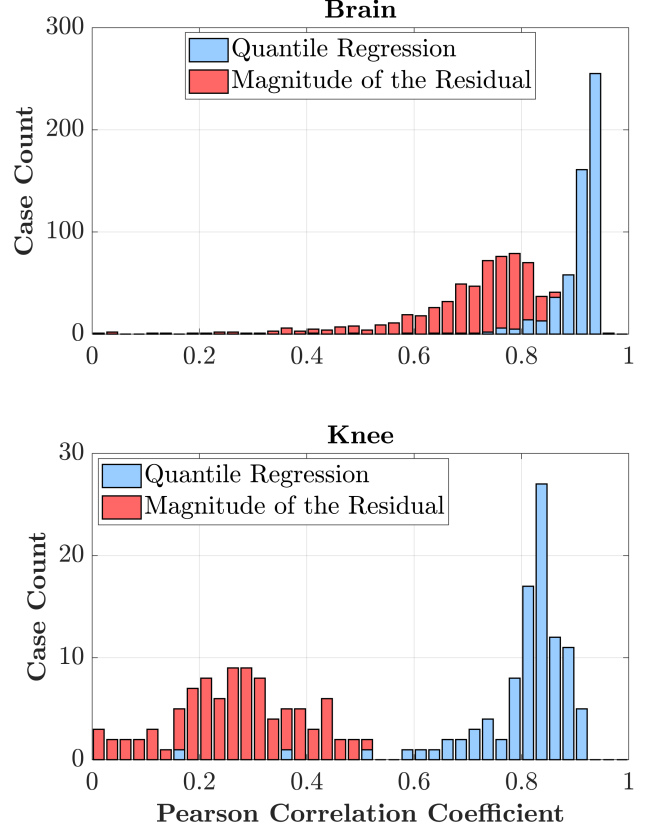


Fig. 3. Distribution of Pearson correlations for the  $4\times$  accelerated brain (top) and knee (bottom) reconstructions. The histograms compare QR-based (blue) and ResM-based (red) uncertainty estimates with the true reconstruction error for each case in the test datasets. QR-based correlations are systematically higher for both anatomies, indicating improved alignment with the true reconstruction error.

#### B. Qualitative assessment of uncertainty

Figure 4 qualitatively compares the absolute reconstruction error (windowed and magnified to enhance visualization) with the QR-based and ResM-based uncertainty maps for a healthy and three abnormal brain cases, respectively at 4-fold undersampling. The blurred maps correspond to the Gaussian-smoothed error and uncertainty maps used for the correlation analysis.

Similarly, Figure 5 compares the absolute reconstruction error (windowed and magnified to enhance visualization) with the QR-based and ResM-based uncertainty maps for three representative knee datasets at 4-fold undersampling.

Figure 6 overlays the QR-based uncertainty map on the reconstructed image for an abnormal brain and highlights the one-to-one correspondence between the uncertainty and pathological regions in the reconstruction.

#### C. Uncertainty as an anomaly detection method

Figure 7 presents uncertainty maps for a healthy and three representative abnormal brains. The uncertainty maps are plotted also using the maximum value from the  $4\times$  accelerated cases as the lower intensity threshold. This was done to show the increase in uncertainty relative to reconstructions for

TABLE II  
CORRELATION BETWEEN UNCERTAINTY AND RECONSTRUCTION ERROR

Acceleration	2×	4×	6×	8×	10×	
Metric (%)	QR	QR	ResM	QR	QR	
<b>Brain</b>						
<b>Pearson</b>	0.82 ± 0.12	0.91 ± 0.10	0.69 ± 0.22	0.92 ± 0.09	0.91 ± 0.09	0.90 ± 0.09
<b>Region-Pearson</b>	0.92 ± 0.12	0.96 ± 0.11	0.73 ± 0.27	0.97 ± 0.09	0.97 ± 0.10	0.97 ± 0.09
<b>Spearman</b>	0.70 ± 0.18	0.76 ± 0.18	0.63 ± 0.22	0.76 ± 0.18	0.77 ± 0.18	0.77 ± 0.19
<b>Region-Spearman</b>	0.75 ± 0.20	0.79 ± 0.22	0.54 ± 0.31	0.84 ± 0.20	0.86 ± 0.19	0.87 ± 0.18
<b>Knee</b>						
<b>Pearson</b>	-	0.80 ± 0.16	0.24 ± 0.27	0.82 ± 0.15	-	-
<b>Region-Pearson</b>	-	0.89 ± 0.17	0.16 ± 0.36	0.91 ± 0.17	-	-
<b>Spearman</b>	-	0.72 ± 0.20	0.26 ± 0.25	0.75 ± 0.20	-	-
<b>Region-Spearman</b>	-	0.79 ± 0.23	0.12 ± 0.34	0.81 ± 0.23	-	-

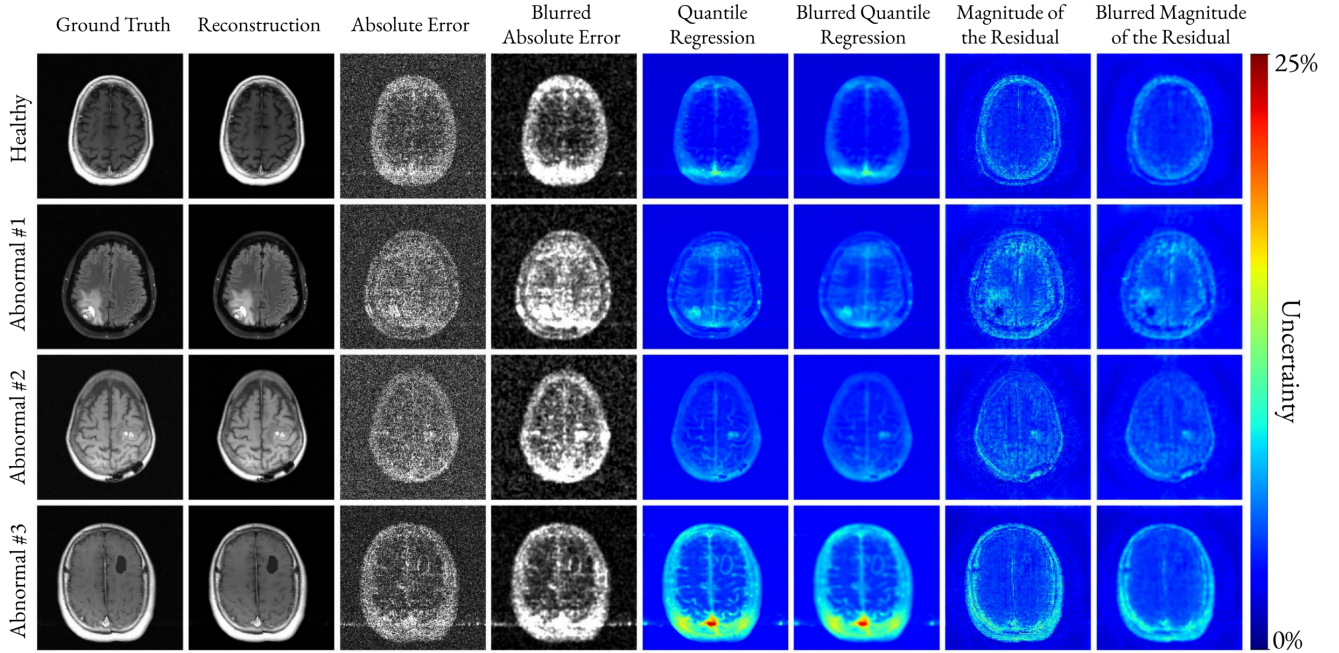


Fig. 4. Comparison between the windowed absolute error (magnified 50 times), the QR-based, and the ResM-based uncertainty for one healthy and three abnormal brain cases. All reconstructions were performed with four-fold acceleration. Blurred versions of the error and the uncertainties, generated by Gaussian smoothing, are also shown. The QR-based uncertainty closely matches the absolute error distribution and in the abnormal cases it delineates the lesions, demonstrating superior localization of uncertainty compared to ResM.

acceleration factors that were considered clinically valid in 100% of the studied cases [16]. Similarly, Figure 8 presents thresholded uncertainty maps for three representative knees. In the bottom panel, the uncertainty maps were thresholded using the maximum value from the 4× accelerated reconstructions.

#### IV. DISCUSSION

Accelerated image reconstruction is one of the most transformative developments in MRI and perhaps the clearest example of an academic innovation that has successfully transitioned into widespread clinical use. Unrolled reconstruction models, such as the E2E VarNet, build directly on the principles of traditional accelerated imaging and have reduced scan times even more. Despite their success, these methods remain neural-network-based, and there is currently no mechanism to verify the accuracy of their outputs or detect hallucinated

structures, particularly at higher acceleration factors where errors are expected [16]. In this work, we introduce an uncertainty quantification framework designed to estimate the reliability of reconstructed images for any acceleration factor.

Table I shows that QR-based uncertainty spans a similar numerical range with ResM. However, the qualitative comparison in Figures 4 and 5 demonstrates that QR provides uncertainty maps that more faithfully mirror the absolute reconstruction error distribution. For the healthy brain in Figure 4, QR highlights the noisy posterior region where the reconstruction error is elevated, whereas ResM produces uniformly high uncertainty around the entire brain, inconsistent with the spatial distribution of the error. If we assume that the reconstruction error is larger in areas with pathologies, since the models were trained with cases representing only a limited number of possible brain lesions, then this suggests that the uncertainty

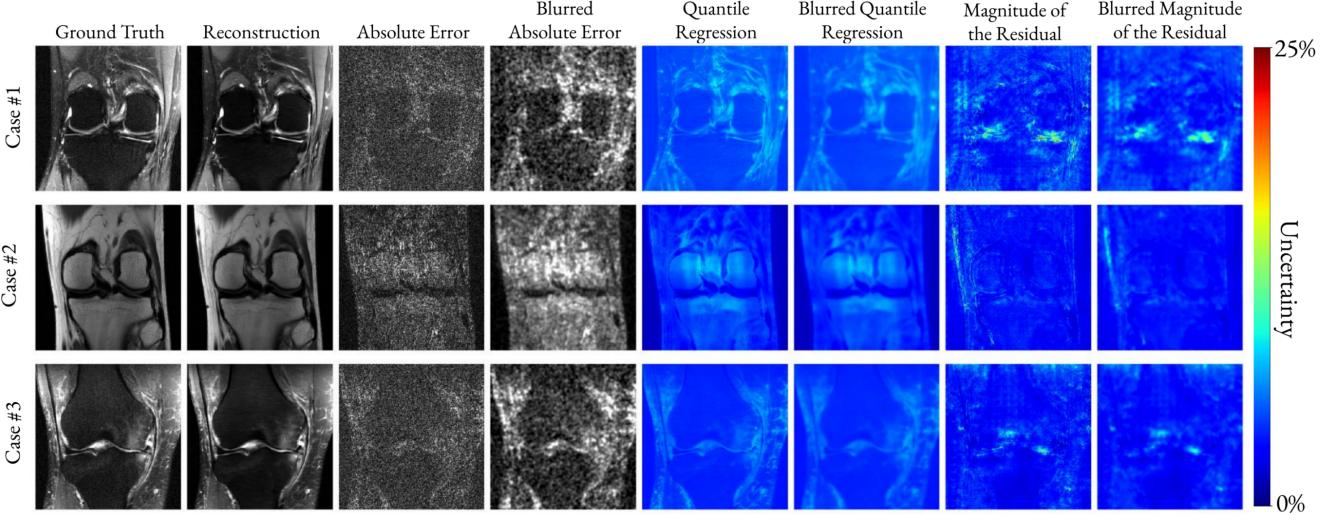


Fig. 5. Comparison between the windowed absolute error (magnified 50 times), the QR-based, and the ResM-based uncertainty for three knees. All reconstructions were performed with four-fold acceleration. Blurred versions of the error and the uncertainties, generated by Gaussian smoothing, are also shown. The QR-based uncertainty qualitatively matches the absolute error distribution unlike the ResM-based approach.

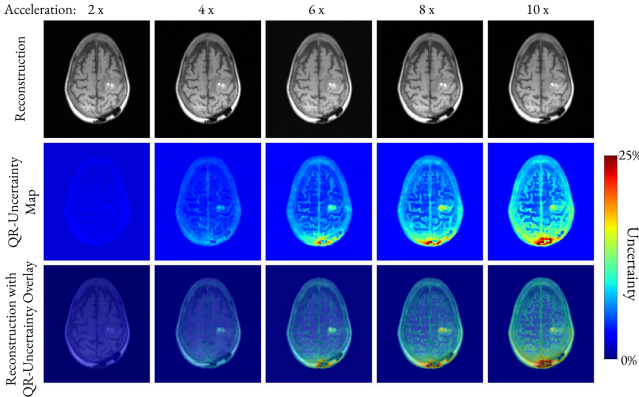


Fig. 6. Reconstructed images and corresponding QR-based uncertainty maps for one abnormal brain for five acceleration factors. Starting at four-fold acceleration, the QR-based uncertainty increases at the location of the lesion and reflects the posterior susceptibility artifact from a prior craniotomy. The bottom row overlays the uncertainty heatmaps on the corresponding reconstructed images to better illustrate that regions of high uncertainty spatially coincide with the lesion and the susceptibility artifact.

values should be higher in correspondence of pathologies. However, we found that while both methods capture global reconstruction noise patterns, only QR consistently highlights the lesion location and structure. In the first abnormal brain, the ResM-based uncertainty in the lesion is low, where the reconstruction error is large and vice-versa. On the other hand, the QR-based uncertainty maps have higher values at the location of the lesions and follows the spatial pattern of the reconstruction error. In the second abnormal brain, the lesion is highlighted by both methods, though its morphology is slightly distorted in ResM. In the third abnormal brain, QR captures the boundary of the treated region, which is lost in the ResM estimate.

Table II further supports these observations by quantifying the relationship between the estimated uncertainty and the

true reconstruction error calculated with fully-sampled ground truth reconstructions. After conformal calibration, the QR-based uncertainty show high Pearson correlations (roughly 90%) with the reconstruction error in brain images for 4-fold acceleration and higher, indicating strong agreement between uncertainty and error magnitude. These high correlations show that the calibrated QR uncertainty scales proportionally with the underlying reconstruction error across the image. For the ResM-based uncertainty, the correlation dropped to 69%. According to the histogram in Figure 3, Pearson correlation is higher when QR is used over ResM. For the reconstructed knee images, the ResM-based uncertainty correlates poorly with the true reconstruction error (Pearson correlation  $< 25\%$ ) due to the smaller calibration dataset (50 volumes comparing to 689 used in the brain) [22].

Pearson correlations are consistently higher than Spearman because magnitude alignment is stronger than strict pixelwise rank ordering, which is more sensitive to local fluctuations in low-error regions. The lower correlations observed at 2-fold acceleration are expected, as the reconstruction error in this regime is small and spatially homogeneous, yielding insufficient dynamic range for a meaningful correlation analysis.

The spatial correspondence between the lesions and regions of high uncertainty is clearly shown by overlaying the QR-based uncertainty heatmap on the reconstructed images (Figure 6). At two-fold acceleration, the uncertainty is near zero and therefore uninformative, which is expected given the high reconstruction accuracy of E2E VarNet at low acceleration factors [1]. At higher accelerations, however, the uncertainty increases, especially in the area of the pathology and in the area affected by the posterior susceptibility artifact from the prior craniotomy. Notably, the regions of elevated uncertainty precisely overlap with the true lesion locations, indicating that the QR-based uncertainty behaves as a trustworthy indicator of reconstruction reliability. Furthermore, this alignment suggests that the QR-based uncertainty can serve as a surrogate for

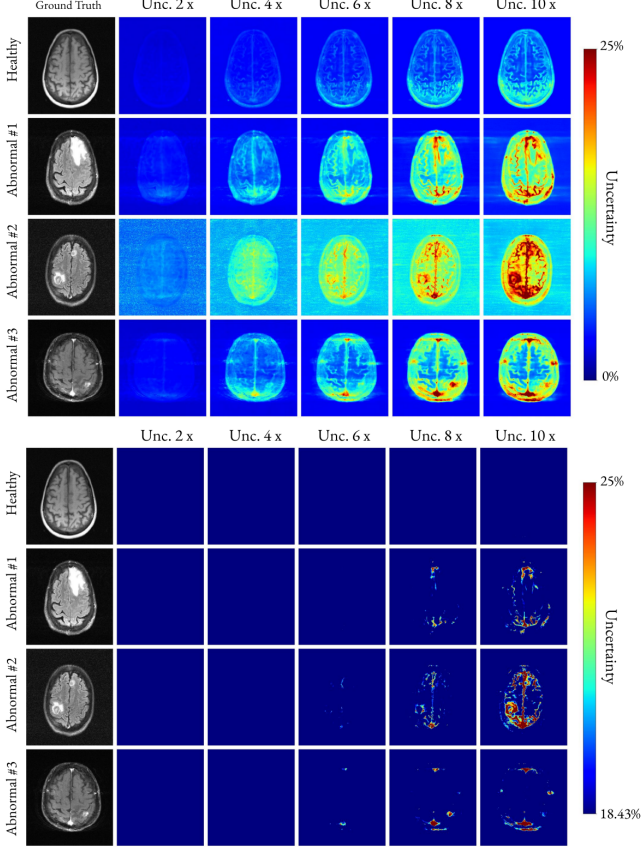


Fig. 7. QR-based uncertainty maps for a healthy brain and three abnormal brain cases across increasing acceleration factors. For each case, uncertainty maps are shown for 2, 4, 6, 8, and 10× acceleration to illustrate how uncertainty evolves with undersampling. **Top:** unthresholded uncertainty maps (lower bound set to zero). **Bottom:** uncertainty maps thresholded using the maximum uncertainty observed at 4× acceleration. Thresholding highlights regions of elevated uncertainty at higher accelerations, corresponding to lesions and post-treatment effects. Note that the background color of abnormal case 3 in the top panel, appears brighter and noisier compared the other three cases. This is expected as there is a higher level of background noise corrupting the ground-truth, and the model is uncertain about its distribution.

reconstruction error during scan time, when fully sampled data are unavailable.

Unrolled network architectures, such as the E2E VarNet, maintain clinical reliability for up to four-fold acceleration [16]. For this reason, in Figures 7 and 8, we used the maximum uncertainty value from the four-fold accelerated reconstructions as a threshold to evaluate higher-acceleration factor reconstructions. In Figure 7, the healthy brain example shows uncertainty below the threshold at 10× acceleration, suggesting that certain slices from healthy studies could be reconstructed safely using very high acceleration factors agreeing with the findings in [16]. In the first abnormal case, uncertainty at 6× undersampling remains below the threshold as well, indicating that some lesions may still be reconstructed accurately with fewer k-space samples than the conventional four-fold limit. In contrast, abnormal cases 2 and 3 exhibit elevated uncertainty near the lesions or in noisy regions at 6× undersampling, implying that these slices should not be acquired with more than 4× undersampling to ensure reliable reconstruction. The results of Figures 7 suggest that a highly

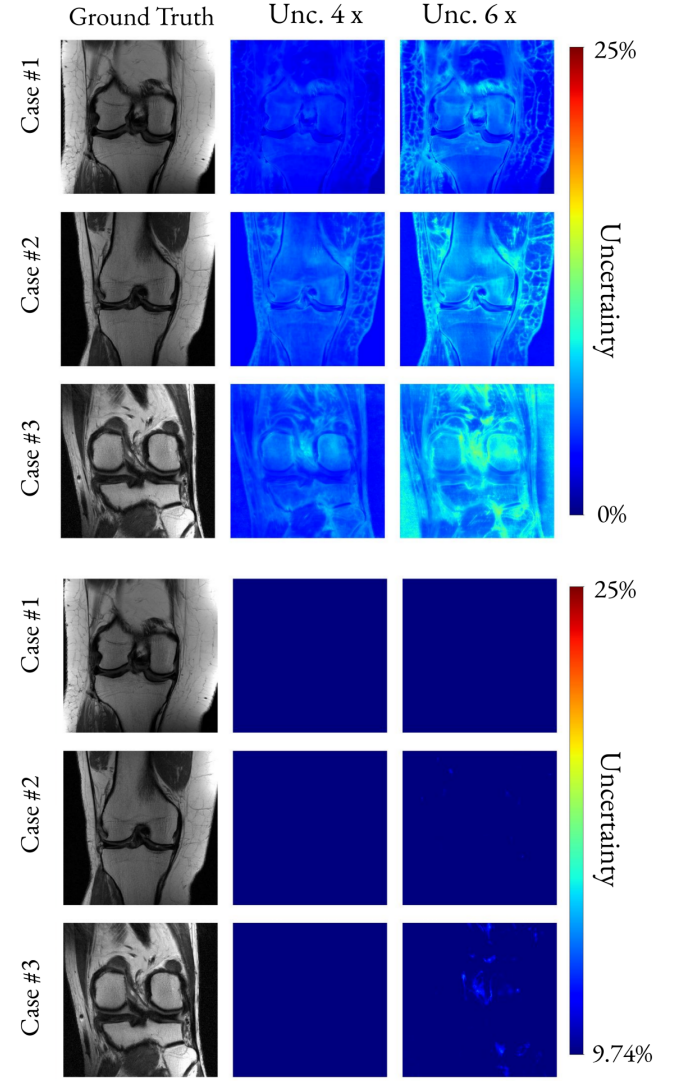


Fig. 8. QR-based uncertainty maps for three knee cases at increasing acceleration. For each case, uncertainty maps are shown for 4 and 6× acceleration to illustrate how uncertainty changes with undersampling in knee MRI. **Top:** unthresholded uncertainty maps (lower bound set to zero). **Bottom:** uncertainty maps thresholded using the maximum uncertainty observed at 4× acceleration. Thresholding highlights regions where uncertainty exceeds levels associated with clinically reliable reconstructions.

accelerated scan—such as a 10× accelerated acquisition—could be used as a rapid anomaly detector or pre-scan to determine whether a longer, diagnostic-quality scan is necessary.

Conformal prediction has a few practical limitations. First, it requires a relatively large and in-distribution held-out calibration set; otherwise, the calibrated bounds may not accurately reflect the true reconstruction error. This is evident from the lower uncertainty values for the knee experiments (50 calibration volumes and maximum uncertainty roughly equal to 15%) compared to the brain (689 calibration volumes and maximum uncertainty roughly equal to 25%). Second, conformal prediction produces per-pixel uncertainty intervals but does not directly provide a mechanism for automatically selecting or controlling the acceleration factor. Integrating uncertainty with decision rules for adaptive sampling therefore

requires additional components beyond conformal prediction alone, which will be investigated in future work. Future work will also incorporate the predicted uncertainty maps into the reconstruction pipeline to selectively refine high-uncertainty areas and potentially improve SSIM performance at higher accelerations.

## V. CONCLUSION

In this work, we introduced conformal QR to quantify the uncertainty of accelerated MRI reconstruction methods in the absence of ground-truth references. Our results demonstrate that QR provides a faithful surrogate for reconstruction error, with strong agreement in both magnitude and spatial distribution across contrasts and acceleration factors. QR-based uncertainty consistently highlights pathological regions and reconstruction failures that are missed by simpler heuristic notions of uncertainty. Since uncertainty increases with undersampling and is higher in regions with pathologies, it could be combined with highly accelerated scans for rapid anomaly detection. More broadly, real-time access to uncertainty information could enable adaptive sampling strategies in which the scanner acquires additional k-space lines only when needed, thereby optimizing scan efficiency while preserving diagnostic quality.

## ACKNOWLEDGMENTS

The authors thank Dr. Tsui-Wei (Lily) Weng for valuable discussions.

## REFERENCES

- A. Sriram *et al.*, “End-to-end variational networks for accelerated MRI reconstruction,” in *International conference on medical image computing and computer-assisted intervention*. Springer, 2020, pp. 64–73.
- D. K. Sodickson and W. J. Manning, “Simultaneous acquisition of spatial harmonics (SMASH): fast imaging with radiofrequency coil arrays,” *Magnetic resonance in medicine*, vol. 38, no. 4, pp. 591–603, 1997.
- K. P. Pruessmann, M. Weiger, M. B. Scheidegger, and P. Boesiger, “SENSE: sensitivity encoding for fast MRI,” *Magnetic Resonance in Medicine: An Official Journal of the International Society for Magnetic Resonance in Medicine*, vol. 42, no. 5, pp. 952–962, 1999.
- M. A. Griswold *et al.*, “Generalized autocalibrating partially parallel acquisitions (GRAPPA),” *Magnetic Resonance in Medicine: An Official Journal of the International Society for Magnetic Resonance in Medicine*, vol. 47, no. 6, pp. 1202–1210, 2002.
- M. Lustig, D. Donoho, and J. M. Pauly, “Sparse MRI: The application of compressed sensing for rapid MR imaging,” *Magnetic Resonance in Medicine: An Official Journal of the International Society for Magnetic Resonance in Medicine*, vol. 58, no. 6, pp. 1182–1195, 2007.
- M. Uecker, T. Hohage, K. T. Block, and J. Frahm, “Image reconstruction by regularized nonlinear inversionjoint estimation of coil sensitivities and image content,” *Magnetic Resonance in Medicine*, vol. 60, no. 3, pp. 674–682, 2008.
- K. Hammernik *et al.*, “Learning a variational network for reconstruction of accelerated MRI data,” *Magnetic resonance in medicine*, vol. 79, no. 6, pp. 3055–3071, 2018.
- H. K. Aggarwal, M. P. Mani, and M. Jacob, “MoDL: Model-based deep learning architecture for inverse problems,” *IEEE transactions on medical imaging*, vol. 38, no. 2, pp. 394–405, 2018.
- T. Eo, Y. Jun, T. Kim, J. Jang, H.-J. Lee, and D. Hwang, “KIKI-net: cross-domain convolutional neural networks for reconstructing undersampled magnetic resonance images,” *Magnetic resonance in medicine*, vol. 80, no. 5, pp. 2188–2201, 2018.
- M. Arvinte, S. Vishwanath, A. H. Tewfik, and J. I. Tamir, “Deep J-Sense: Accelerated MRI reconstruction via unrolled alternating optimization,” in *International conference on medical image computing and computer-assisted intervention*. Springer, 2021, pp. 350–360.
- Y. Jun, H. Shin, T. Eo, and D. Hwang, “Joint deep model-based MR image and coil sensitivity reconstruction network (joint-ICNet) for fast MRI,” in *Proceedings of the IEEE/CVF conference on computer vision and pattern recognition*, 2021, pp. 5270–5279.
- I. I. Giannakopoulos *et al.*, “Accelerated MRI reconstructions via variational network and feature domain learning,” *Scientific Reports*, vol. 14, no. 1, p. 10991, 2024.
- M. P. Recht *et al.*, “Using deep learning to accelerate knee MRI at 3 T: results of an interchangeability study,” *American Journal of Roentgenology*, vol. 215, no. 6, pp. 1421–1429, 2020.
- D. J. Lin, P. M. Johnson, F. Knoll, and Y. W. Lui, “Artificial intelligence for MR image reconstruction: an overview for clinicians,” *Journal of Magnetic Resonance Imaging*, vol. 53, no. 4, pp. 1015–1028, 2021.
- P. M. Johnson *et al.*, “Deep learning reconstruction enables prospectively accelerated clinical knee MRI,” *Radiology*, vol. 307, no. 2, p. e220425, 2023.
- A. Radmanesh *et al.*, “Exploring the acceleration limits of deep learning variational network-based two-dimensional brain MRI,” *Radiology: Artificial Intelligence*, vol. 4, no. 6, p. e210313, 2022.
- P. M. Johnson *et al.*, “Prostate Cancer Risk Stratification and Scan Tailoring Using Deep Learning on Abbreviated Prostate MRI,” *Journal of Magnetic Resonance Imaging*, 2025.
- S. Bhadra, V. A. Kelkar, F. J. Brooks, and M. A. Anastasio, “On hallucinations in tomographic image reconstruction,” *IEEE transactions on medical imaging*, vol. 40, no. 11, pp. 3249–3260, 2021.
- S. Kiryu *et al.*, “Clinical impact of deep learning reconstruction in MRI,” *Radiographics*, vol. 43, no. 6, p. e220133, 2023.
- A. Kendall and Y. Gal, “What uncertainties do we need in bayesian deep learning for computer vision?” *Advances in neural information processing systems*, vol. 30, 2017.
- M. Abdar *et al.*, “A review of uncertainty quantification in deep learning: Techniques, applications and challenges,” *Information fusion*, vol. 76, pp. 243–297, 2021.
- A. N. Angelopoulos *et al.*, “Image-to-image regression with distribution-free uncertainty quantification and applications in imaging,” in *International Conference on Machine Learning*. PMLR, 2022, pp. 717–730.
- V. Edupuganti, M. Mardani, S. Vasanawala, and J. Pauly, “Uncertainty quantification in deep MRI reconstruction,” *IEEE Transactions on Medical Imaging*, vol. 40, no. 1, pp. 239–250, 2020.
- R. Tanno *et al.*, “Uncertainty quantification in deep learning for safer neuroimage enhancement,” *arXiv preprint arXiv:1907.13418*, 2019.
- D. Narnhofer, A. Effland, E. Köbler, K. Hammernik, F. Knoll, and T. Pock, “Bayesian uncertainty estimation of learned variational MRI reconstruction,” *IEEE transactions on medical imaging*, vol. 41, no. 2, pp. 279–291, 2021.
- M. Ekanayake, K. Pawar, Z. Chen, G. Egan, and Z. Chen, “PixCUE: joint uncertainty estimation and image reconstruction in MRI using deep pixel classification,” *Journal of Imaging Informatics in Medicine*, vol. 38, no. 4, pp. 2071–2084, 2025.
- K. Wang *et al.*, “Rigorous uncertainty estimation for MRI reconstruction,” in *Proceedings of the proceedings of the 30th annual meeting of ISMRM*, vol. 749, 2022.
- P. Fischer, J. N. Morshuis, T. Küstner, and C. Baumgartner, “CUTE-MRI: Conformalized Uncertainty-based framework for Time-adaptive MRI,” *arXiv preprint arXiv:2508.14952*, 2025.
- J. Zbontar *et al.*, “fastMRI: An open dataset and benchmarks for accelerated MRI,” *arXiv preprint arXiv:1811.08839*, 2018.
- F. Knoll *et al.*, “fastMRI: A publicly available raw k-space and DICOM dataset of knee images for accelerated MR image reconstruction using machine learning,” *Radiology: Artificial Intelligence*, vol. 2, no. 1, p. e190007, 2020.
- O. Ronneberger, P. Fischer, and T. Brox, “U-net: Convolutional networks for biomedical image segmentation,” in *International Conference on Medical image computing and computer-assisted intervention*. Springer, 2015, pp. 234–241.
- Z. Wang, E. P. Simoncelli, and A. C. Bovik, “Multiscale structural similarity for image quality assessment,” in *The thirty-seventh asilomar conference on signals, systems & computers, 2003*, vol. 2. Ieee, 2003, pp. 1398–1402.
- R. Koenker and G. Bassett Jr, “Regression quantiles,” *Econometrica: journal of the Econometric Society*, pp. 33–50, 1978.
- Y. Romano, E. Patterson, and E. Candes, “Conformalized quantile regression,” *Advances in neural information processing systems*, vol. 32, 2019.
- P. Chaudhuri, “Global nonparametric estimation of conditional quantile functions and their derivatives,” *Journal of multivariate analysis*, vol. 39, no. 2, pp. 246–269, 1991.

- [36] K. Q. Zhou and S. L. Portnoy, “Direct use of regression quantiles to construct confidence sets in linear models,” *The Annals of Statistics*, vol. 24, no. 1, pp. 287–306, 1996.
- [37] K. Q. Zhou and S. L. Portnoy, “Statistical inference on heteroscedastic models based on regression quantiles,” *Journal of Nonparametric Statistics*, vol. 9, no. 3, pp. 239–260, 1998.
- [38] I. Takeuchi, Q. Le, T. Sears, A. Smola *et al.*, “Nonparametric quantile estimation,” *Journal of Machine Learning Research*, vol. 7, pp. 1231–1264, 2006.
- [39] I. Steinwart and A. Christmann, “Estimating conditional quantiles with the help of the pinball loss,” *Bernoulli*, vol. 17, no. 1, pp. 211–225, 2011.
- [40] S. Bates, A. Angelopoulos, L. Lei, J. Malik, and M. Jordan, “Distribution-free, risk-controlling prediction sets,” *Journal of the ACM (JACM)*, vol. 68, no. 6, pp. 1–34, 2021.
- [41] W. Hoeffding, “Probability inequalities for sums of bounded random variables,” *Journal of the American statistical association*, vol. 58, no. 301, pp. 13–30, 1963.
- [42] K. Pearson, “VII. Note on regression and inheritance in the case of two parents,” *proceedings of the royal society of London*, vol. 58, no. 347–352, pp. 240–242, 1895.
- [43] C. Spearman, ““General Intelligence” Objectively Determined and Measured.” *The American Journal of Psychology*, vol. 15, no. 2, pp. 201–293, 1904.